Heliyon 10 (2024) e28609

Contents lists available at ScienceDirect

Heliyon

journal homepage: www.cell.com/heliyon

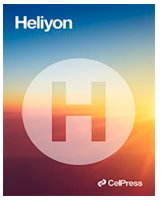

Research article

Artificial neural network (ANN) analysis on thermophysical properties of magnetohydrodynamics flow with radiation in an arc-shaped enclosure with a rotating cylinder

T. Bairagi [a], Md. Jahid Hasan [b], M.N. Hudha [a], A.K. Azad [c], M.M. Rahman [a,*]

[a] Department of Mathematics, Bangladesh University of Engineering and Technology, Dhaka, 1000, Bangladesh
[b] Department of Mechanical and Production Engineering, Islamic University of Technology, Board Bazar, Gazipur, 1704, Bangladesh
[c] Department of Natural Sciences, Islamic University of Technology, Board Bazar, Gazipur, 1704, Bangladesh

ARTICLE INFO

Keywords:
Artificial neural network
Two-layer feed-forward model
Lid-driven arc-shaped cavity
Rotating cylinder
Water-based Al_2O_3 nanofluid

ABSTRACT

The objective of this research is to examine the thermophysical features of magnetic parameter (*Ha*) and time step (τ) in a lid-driven cavity using a water-based Al_2O_3 nanofluid and the efficacy of ANN models in accurately predicting the average heat transfer rate. The Galerkin weighted residual approach is used to solve a set of dimensionless nonlinear governing equations. The Levenberg-Marquardt back propagation technique is used for training ANN using sparse simulated data. The findings of the investigation about the flow and thermal fields are shown. Furthermore, a comparative study and prediction have been conducted on the impact of manipulating factors on the average Nusselt number derived from the numerical heat transfer analysis. The findings of the research indicate that, in the absence of magnetohydrodynamics, a rise in the Hartmann number resulted in a drop in both the fluid velocity profile and magnitude. Conversely, it was observed that the temperature and Nusselt number exhibited an increase under these conditions. The mean temperature of the fluid rises as the Hartmann number drops, reaching a peak value of 0.114 when $Ha = 0$. The scenario where $Ha = 0$, representing the lack of magnetohydrodynamics, shows the highest average Nusselt number, whereas the instance with $Ha = 45$ presents the lowest Nusselt number. The ANN model has a high level of accuracy, as seen by an MSE value of 0.00069 and a MAE value of 0.0175, resulting in a 99% accuracy rate.

1. Introduction

The enhancement of heat transfer in a lid-driven cavity subjected to mixed convection has been a prominent subject of investigation in previous decades. This issue is significant in several industrial applications, including microfluidics, heat exchangers, electronics cooling, solar energy, and renewable energy systems [1]. Azeez et al. [2] investigated the double-diffusive mixed convection in a lid-driven cavity using MWCNT/water varying the Reynolds number (Re), Richardson number (Re), Hartmann number (*Ha*), volume fractions, etc. They observed that the heat and mass transfer characteristics improve with the augment of Ri. The numerical investigation conducted by Alsabery et al. [3] examined the impact of partial slip on a square cavity, using aluminum oxide nanofluid. They observed that an augment in the Ri corresponds to an increase in the Nusselt number (*Nu*). The study conducted by Kashyap and Dass

* Corresponding author.
E-mail address: mmustafizurrahman@math.buet.ac.bd (M.M. Rahman).

https://doi.org/10.1016/j.heliyon.2024.e28609
Received 13 November 2023; Received in revised form 5 February 2024; Accepted 21 March 2024
Available online 24 March 2024

Nomenclature

B_0	Magnetic field induction (T)
C_p	Specific heat at constant pressure ($Jkg^{-1}K^{-1}$)
h	Convective heat transfer coefficient ($Wm^{-2}K^{-1}$)
H	Length of the enclosure (m)
k	Thermal conductivity of the material ($Wm^{-1}K^{-1}$)
p	Dimensional pressure (Nm^{-2})
ψ	Stream function
t	Dimensional time (s)
Pr	Prandtl number
Ri	Richardson number
Rd	Radiation parameter

Greek Symbols

α	Thermal diffusivity (m^2s^{-1})
β	Co-efficient of thermal expansion (K^{-1})
ρ	Density of the material (kgm^{-3})
σ	Electrical conductivity ($\Omega^{-1}m^{-1}$)
σ_e	Stefan-Boltzmann constant
κ	Permeable parameter
θ	Dimensional temperature (K)
Θ	Dimensionless temperature
φ	Solid volume fraction
μ	Dynamic viscosity of the fluid ($kgm^{-1}s^{-1}$)
ω_0	Dimensional rotation speed of the cylinder (rad/s)
q_R	Radiative heat flux
P	Dimensionless pressure
x, y	Dimensional cartesian coordinates
X, Y	Dimensionless cartesian coordinates
u, v	Dimensional velocity components (ms^{-1})
U, V	Dimensionless velocity components
g	Acceleration due to gravity (ms^{-1})
Nu	Nusselt number
Gr	Grashoff number
Ha	Hartmann number
Re	Reynolds number
ω	Dimensionless rotation speed of the cylinder
ν	Kinematic viscosity of the fluid (m^2s^{-1})
τ	Dimensionless time (s)

Subscripts

av	average
f	fluid
h	hot
c	cold
nf	nanofluid
p	solid particle
s	solid

[4] examined the impact of cavity inclination on mixed convection, using various Richardson values. The researchers' results provide clarification that the angle of inclination has a significant impact on both entropy formation and heat transport. Yaseen et al. [5] assessed the effects of lid-driven flow on mixed convection by using the finite element approach and manipulating the Richardson and Reynolds numbers. Their findings indicate that there is an augment in the heat transmission rate ranging from 4.5% to 28% across various wall motions. Yeasmin et al. [6] examined the thermal and fluid phenomena occurring in an L-shaped lid-driven hollow. They specifically investigated the use of kerosene-alumina nanofluid and used the Galerkin residual approach for their analysis. The findings of their study demonstrated a favorable correlation between the Reynolds number and Darcy number, and the temperature distribution and fluid velocity profile inside the cavity.

Nanofluids are widely used in different industries for enhancing the heat transfer rate and have become one of the most popular topics in research. It has become trendy due to its high thermal conductivity and energy efficiency. Zang et al. [7] did a study on the

mixed convection in a semi-elliptic cavity flow under mixed convection using water-silver nanofluid varying the nanofluid concentrations and Grashoff number. They concluded that with the rise of nanofluid concentrations, the heat transfer rate shoots up significantly. On top of that, the temperature and velocity profile also rise due to the higher Grashoff number. Wang and Xu [8] examined the mixed convection flow in an inclined cavity using hybrid nanofluids by the Coiflet wavelet-homotopy method. They noticed that the hybrid nanofluids perform better than the conventional fluids in terms of thermal enhancement. Hussain et al. [9] carried out the magneto-bioconvection flow in a porous cavity using hybrid nanofluids using the Galerkin finite element method. They declared that the thermal performance lessens with the augment of Darcy number. Batool et al. [10] inspected the thermal and mass transport in an enclosure using a micropolar nanofluid by finite volume approach. Ahmed et al. [11] built a model of convective transport for obtaining heat transfer coefficients for hybrid nanofluid. They successfully modeled for getting the Nusselt number by quadratic multiple regression where the thermophoretic impact is more considered than the Brownian motion. Das et al. [12] conducted research on mixed convective flow in a vertical channel, where they noticed that as the volume proportion of nanoparticles increased, the rate of heat transfer also increased. Furthermore, they discovered that the rate of fluid flow increases as the Rayleigh number increases.

In cavity flow, radiation plays a crucial role in augmenting the heat transfer rate under different conditions. Due to the complex boundary conditions and real-life situations, radiation is considered for modeling heat transfer calculations. The work done by Farooq et al. [13] investigated the flow of a nanofluid, taking into account nonlinear radiation in the presence of magnetohydrodynamics. The researchers concluded that the radiation parameter has a role in augmenting the thickness of the thermal barrier layer. The laminar flow in a vertical channel with variable radiation parameters was explored by Mostafazadeh and Toghraie [14]. The investigation conducted by Sheikholeslami et al. [15] assessed the radiation impact inside an enclosure, including an elliptical cylinder under natural convection. The study used the finite element approach and specifically focused on the utilization of Fe_3O_4 nanofluid. The research revealed a positive correlation between the *Nu* and the radiation parameters, indicating that a rise in the latter leads to an augment in the former. In a separate investigation, Sheikholeslami [16] conducted an assessment of the magnetic influence within the context of radiation and natural convection. The author demonstrated that the thermal transport shoots up as the radiation parameters and buoyancy forces increase. Soomro et al. [17] worked on the effects of nonlinear radiation in a moving slip surface using the finite difference technique. They discovered that both the *Nu* and Sh go up with the rise of the thermal radiation parameter.

Magnetohydrodynamics is a notable consideration while working with the cavity flow under various conditions such as mixed convection, radiation, etc. Barnoon et al. [18] did a study on a cavity under mixed convection and magnetohydrodynamics. The results revealed that the thermal performance shoots up with the rise of solid volume fraction and the reduction of the *Ha* and Ri. Çolak et al. [19] examined the impact of MHD in a chamfered cavity using OpenFOAM varying the Ri, *Ha*, and magnetic source inclination angle. Korei et al. [20] inspected the magnetic effect in a cavity where Al_2O_3–Cu/water hybrid nanofluid is taken as fluid considering the variable Ri, *Ha*, and concentrations. They observed that the inclination angle highly affects the heat transfer performance in the cavity. Nasrin and Parvin [21] evaluated the unsteady mixed convection considering the magnetic impact in a cavity with a sinusoidal wavy wall. They concluded that the Hartmann number and Reyleigh number act opposite in terms of thermal performance and fluid phenomena. Selimefendigil and Öztop [22] considered an L-shaped cavity under MHD mixed convection with the existence of external heat generations varying the Reighleigh number, *Ha*, Ri, inclination angle, and aspect ratio. The results elucidated that the magnetic inclination angle greatly affects changing the thermal transport, considering other parameters to be constant. Das et al. [23] worked on the unsteady magneto-buoyancy driven flow using eater ethylene glycol nanofluid. They found that Hall currents tend to enhance the vertical fluid flow and reduce the magnitude of the fluid velocity in the cross-flow direction. In another study [24], they worked on the gyrating channel filled with reactive second-grade nanofluid and declared that the Hall currents have a substantial impact on the flow dynamics and thermal characteristics of the gyratory motion. Shafiq et al. [25] assessed the bioconvection flow of second-grade nanofluid with gyrotactic microorganisms using Artificial Neural Network (ANN). They observed that when the thermophoretic parameter is big, both the concentration of nanoparticles and the distribution of temperature rise.

The rotational movement of mechanical parts in a chamber or machinery region is usually seen in heat transfer applications. Many researchers consider rotating cylinders in the cavity flow to assess the additional impact of the movement of the fluid along with the moving lid. Chatterjee et al. [26] did a study on a cavity using Cu-water nanofluid with a rotating cylinder at the center varying the Richardson number, rotational speed, and Grashoff number. They concluded that the heat transfer is highly dependent upon the rotational speed of the moving cylinder. Kareem and Gao [27] inspected the mixed convective heat transfer phenomena in a cavity with a rotating cylinder for different Reynolds numbers using Large Eddy Simulation (LES). They also declared that the heat transfer performance depends on the cylinder's rotational speed or the Reynolds number. Khanafer and Aithal [28] evaluated the thermal performance and fluid flow phenomena in a lid-driven cavity with a rotational cylinder under mixed convection. They noticed that the *Nu* rises with the augment of angular velocity and the highest thermal transport is found when there is the rotational cylinder is placed inside the cavity. Imtiaz et al. [29] assessed the influence of heat generation in a cavity under mixed convection considering a rotating cylinder changing the Re, Ri, and Grashoff numbers. They noticed that when the velocity of the lid rises, the effect of heat generation on the cavity reduces, resulting in lower temperature distribution. In a separate investigation, Selimefendigil and Oztop [30] worked on mixed convective cavity flow considering two rotating cylinders using the finite element method varying the Reynolds number, angular velocity, and diameter ratio. They observe that the moving cylinders augment the heat transfer rate by 181.5% in the cavity compared to the case of the non-rotating cylinders.

Artificial neural network (ANN) analysis has recently been introduced in order to optimize the solution [31–35]. Various researchers implemented ANN to solve the problems of heat transfer and fluid flow. Çolak et al. [36] worked on the reliability study of the Rayleigh distribution and inverse power law to implement a new model of ANN. Shafiq et al. [37] investigated the Darcy–Forchheimer Tangent hyperbolic flow in a cylindrical surface utilizing ANN. The rheological features are examined for both

Newtonian and tangent hyperbolic fluid scenarios in order to have a better understanding of the results. Shafiq et al. [38] analyzed the distribution's behaviour by employing the Maximum Likelihood Estimation (MLE) technique to estimate its parameters. Additionally, the study aims to identify the most effective ANN method by comparing it to the maximum likelihood estimation method. The ANN method will be applied to actual data from breast cancer patients to determine survival rates, risk factors, and other survival study functions associated with the log-logistic distribution. Sindhu et al. [39] investigated the multilayer ANN with Bayesian regularization modelling for reliability metrics of the generalized exponential model. Several studies have been carried out analyzing the problems on SWCNT nanofluid, Williamson nanofluid, Ree–Eyring fluid with chemical reaction, exponentiated Weibull distribution etc., using the ANN algorithm [40–43].

The literature review reveals that numerous studies have been conducted on mixed convective flow in a lid-driven cavity, involving MHD, nanofluids, radiation, and a rotating cylinder. However, no research has been conducted in which the ANN model is used to predict the average heat transfer rate due to the thermophysical properties of magnetohydrodynamics on an arc-shaped cavity with a rotating cylinder using nanofluid and radiative heat flux. This study aims to assess the impacts of MHD on heat transfer and fluid flow phenomena using a feed-forward back propagation neural network model. A comparative study and prediction of the average Nusselt number, obtained from a numerical study, were conducted by using a neural network model to investigate the influence of regulating factors. The Levenberg-Marquardt backpropagation algorithm is employed for training an ANN using sparse simulated data. The ANN architecture consists of two hidden layers, with the first hidden layer containing 15 neurons and the second hidden layer containing five neurons. The activation function used for the first hidden layer is the rectified linear unit (ReLU), while the second hidden layer utilizes the Tangent Hyperbolic (Tanh) activation function. MHD flow with radiation in an arc-shaped cage with a spinning cylinder has several engineering and industrial uses. One example is designing and optimizing electromagnetic pumps for liquid metal circulation in metallurgical industries. Heat transmission and fluid flow are improved by MHD. In the cooling systems of advanced nuclear reactors, magnetic fields, fluid flow, and thermal radiation affect reactor efficiency and safety. Aerospace technology depends on studying MHD flow and radiation in arc-shaped enclosures with spinning cylinders. This research affects magnetohydrodynamic thrust-producing spacecraft propulsion systems. Understanding and using these complex fluid dynamics phenomena in various industrial and technological domains can improve engineering efficiency, safety, and performance. The findings of this research will contribute to the development of mechanical systems that include the principles of heat transfer in the presence of mixed convection, radiation, and magnetohydrodynamics. This discovery has the potential to greatly help the fields of heat transfer, nanomaterials, industrial components design, and the microfluidics community.

2. Mathematical specification

2.1. Physical model

The physical representation of this problem entails a square cavity with a length H that is filled with a nanofluid composed of water and Al_2O_3, as seen in Fig. 1. The flow under consideration is characterized as a Newtonian unstable laminar mixed convection flow,

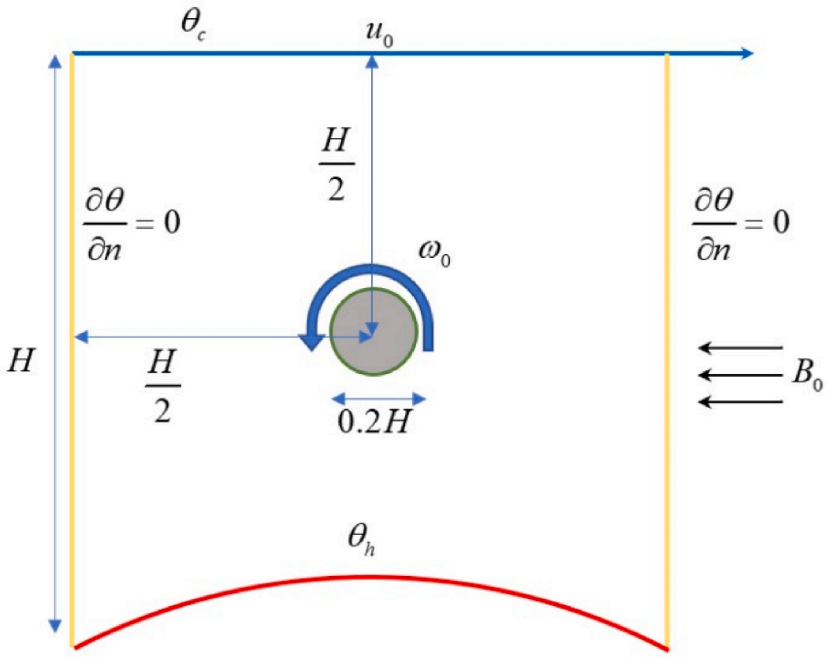

Fig. 1. Physical model of the body with boundary conditions and dimensions.

taking into account the influence of a magnetic field and the radiative properties of the medium. The water molecules and Al_2O_3 nanoparticle forms exhibit a uniform and consistent morphology and size, and are in a state of thermal equilibrium, with no relative motion or slide occurring between the two mediums. The lower wall of the hollow exhibits an arc form with a radius of H. The virtual center of the arc is positioned equidistantly from both of the bottom corners of the cavity. So, the virtual center of the arc is, $\left(\frac{H}{2}, -\frac{H\sqrt{3}}{2}\right)$, as mentioned before the radius of the arc is H. A conductive solid cylinder of diameter is placed in the middle of the cavity and undergoes counterclockwise rotation with rotational speed $\omega = 5$. The top wall is kept at a constant low temperature (θ_c), moving with a uniform velocity of u_0, all other walls are stationary. The bottom arc-shaped wall is kept at a constant high temperature (θ_h) and both sidewalls are thermally insulated ($\theta_h > \theta_c$). A homogeneous magnetic field is applied to the right-side wall of the cavity, with the magnetic field lines oriented perpendicular to the right wall in a leftward orientation.

2.2. Governing equations

The governing equations used for this numerical study have been given as follows based on [44]:
Continuity equation

$$\rho_{nf}(\nabla \cdot \mathbf{u}) = 0 \tag{1}$$

Momentum equations

$$\rho_{nf}\left\{\frac{\partial \mathbf{u}}{\partial t} + (\mathbf{u}\cdot\nabla)\mathbf{u}\right\} = -\nabla \cdot p + \mu_{nf}\nabla^2\mathbf{u} + \mathbf{F} \tag{2}$$

Energy equation for nanofluid

$$\left(\rho C_p\right)_{nf}\left(\frac{\partial \theta}{\partial t} + \mathbf{u}\cdot\nabla\theta\right) = k_{nf}\nabla^2\theta - \nabla \cdot q_R\mathbf{I} \tag{3}$$

Equation for solid region

$$\frac{\partial \theta_s}{\partial t} = k_s\nabla^2\theta_s \tag{4}$$

Where $\mathbf{u} = (u,v)^T\mathbf{F} = (0, (\rho\beta)_{nf}g(\theta - \theta_c) - \sigma_{nf}{B_0}^2v)^T\mathbf{I} = (\hat{i},\hat{j})^T$ and k_s is the thermal conductivity of the solid cylinder.
With boundary conditions

$$\left.\begin{array}{c} t = 0, u = v = \theta = p = 0 \\ t > 0, u = v = 0, \theta = \theta_h \text{ along } \left(x - H/2\right)^2 + \left(y + \sqrt{3}H/2\right)^2 = H^2, [y \geq 0] \\ u = u_0, v = 0, \theta = \theta_c \text{ along } y = H; 0 \leq x \leq H \\ u = v = \dfrac{\partial \theta}{\partial x} = 0, \text{along } x = 0, 1; 0 \leq y \leq H \\ \text{At solid (cylinder) fluid interface, u} = -\omega_0 \sin\theta, v = \omega_0\cos\theta;\ k_f\dfrac{\partial \theta}{\partial n} = k_s\dfrac{\partial \theta_s}{\partial n} \end{array}\right\} \tag{5}$$

2.3. Dimensional analysis

To minimize the computation cost and to introduce dimensionless parameters we've used the proper scaling technique to convert the equations from (1) to (5) into dimensionless form.
The scaling techniques are

$$X = \frac{x}{H}, Y = \frac{y}{H}, \tau = \frac{u_0 t}{H}, U = \frac{u}{u_0}, V = \frac{v}{u_0}, P = \frac{p}{\rho_f {u_0}^2}, \Theta = \frac{\theta - \theta_c}{\theta_h - \theta_c}, \Theta_s = \frac{\theta_s - \theta_c}{\theta_h - \theta_c}, \omega = \frac{\omega_0}{2\pi} \tag{6}$$

2.4. Approximation of the radiative term

The approximation of the term for the radiation effect was done according to the following procedure [45].

$$\left.\begin{array}{l} \text{For } \dfrac{\partial q_R}{\partial x}, q_R = -\dfrac{4\sigma_e}{3\beta_R}\dfrac{\partial \theta^4}{\partial x} \\ \text{and for, } \dfrac{\partial q_R}{\partial y}, q_R = -\dfrac{4\sigma_e}{3\beta_R}\dfrac{\partial \theta^4}{\partial y} \end{array}\right\} \tag{7}$$

Also, θ^4 was approximated by Stefan's law of radiation.

$$\theta^4 \cong 4\theta_c^3\theta - 3\theta_c^4 \tag{8}$$

The radiation parameter used as

$$Rd = \frac{4\sigma_e\theta_c^3}{\beta_R k} \tag{9}$$

Using the aforementioned transformations, the dimensionless set of governing equations has been reduced to the following form.
Continuity equation

$$\frac{\partial U}{\partial X} + \frac{\partial V}{\partial Y} = 0 \tag{10}$$

Momentum equations

$$\frac{\partial U}{\partial \tau} + U\frac{\partial U}{\partial X} + V\frac{\partial U}{\partial Y} = -\frac{\rho_f}{\rho_{nf}}\frac{\partial P}{\partial X} + \frac{\upsilon_{nf}}{\upsilon_f \mathrm{Re}}\left(\frac{\partial^2 U}{\partial X^2} + \frac{\partial^2 U}{\partial Y^2}\right) \tag{11}$$

$$\frac{\partial V}{\partial \tau} + U\frac{\partial V}{\partial X} + V\frac{\partial V}{\partial Y} = -\frac{\rho_f}{\rho_{nf}}\frac{\partial P}{\partial Y} + \frac{\upsilon_{nf}}{\upsilon_f \mathrm{Re}}\left(\frac{\partial^2 V}{\partial X^2} + \frac{\partial^2 V}{\partial Y^2}\right) + \frac{(\rho\beta)_{nf}}{\rho_{nf}\beta_f} Ri\Theta - \frac{\sigma_{nf}\rho_f}{\sigma_f \rho_{nf}}\frac{Ha^2 V}{\mathrm{Re}} \tag{12}$$

Energy equation for nanofluid

$$\frac{\partial \Theta}{\partial \tau} + U\frac{\partial \Theta}{\partial X} + V\frac{\partial \Theta}{\partial Y} = \frac{\alpha_{nf}}{\alpha_f \mathrm{RePr}}\left(1 + \frac{4k_f}{3k_{nf}}Rd\right)\left(\frac{\partial^2 \Theta}{\partial X^2} + \frac{\partial^2 \Theta}{\partial Y^2}\right) \tag{13}$$

Energy equation for solid cylinder

$$\frac{\partial \Theta_s}{\partial \tau} - K\left(\frac{\partial^2 \Theta_s}{\partial X^2} + \frac{\partial^2 \Theta_s}{\partial Y^2}\right) = 0 \tag{14}$$

Where K is the ratio of thermal conductivity of solid cylinder to nanofluid $K = \frac{k_s}{k_{nf}}$.

2.5. Non-dimensional boundary conditions

Now using the same transformation technique, the dimensionless boundary conditions are transformed as

$$\left.\begin{array}{c} \tau = 0, U = V = \Theta = P = 0 \\ \tau > 0, U = V = 0, \Theta = 1 \text{ along bottom wall of the cavity} \\ U = 1, V = \Theta = 0, \text{along moving Lid} \\ U = V = \dfrac{\partial \Theta}{\partial X} = 0, \text{at the sidewalls} \\ \text{At the solid(cylinder) fluid interface,} \\ \mathrm{U} = -\omega(Y - 0.5), V = \omega(X - 0.5), \dfrac{\partial \Theta}{\partial N} = K\dfrac{\partial \Theta_s}{\partial N}, K = \dfrac{k_s}{k_{nf}} \end{array}\right\} \tag{15}$$

2.6. Nanofluid and its properties

These thermophysical properties of the nanofluid are considered as below according to Hasib et al. [46] and presented in Table 1. The properties of nanofluids that are used in equations (10)–(14) will be used according to the following relations.

Table 1
Thermophysical properties of the base fluid and nanoparticles [46].

Properties	Base fluid (Water)	Solid Nanoparticle (AL_2O_3)	Unit
ρ	997.1	3970	kgm^{-3}
C_p	4179	765	$Jkg^{-1}K^{-1}$
k	0.613	40	$Wm^{-1}K^{-1}$
β	21×10^{-5}	85×10^{-7}	K^{-1}
μ	0.001003	–	$kgm^{-1}s^{-1}$
σ	0.05	1×10^{-10}	m^2s^{-1}

The density, specific heat, and viscosity of the nanofluids are used according to the relations [47].

$$\rho_{nf} = (1-\varphi)\rho_f + \varphi\rho_p \tag{16}$$

$$(\rho C_p)_{nf} = (1-\varphi)(\rho C_p)_f + \varphi(\rho C_p)_p \tag{17}$$

$$\mu_{nf} = \mu_{nf}\left(123\varphi^2 + 7.3\varphi + 1\right) \tag{18}$$

The other properties of the nanofluid were taken as below [48].

$$(\rho\beta)_{nf} = (1-\varphi)(\rho\beta)_f + \varphi(\rho\beta)_p - \varphi(1-\varphi)(\rho_p - \rho_f)(\beta_p - \beta_f) \tag{19}$$

$$\sigma_{nf} = \left(1 + \frac{3(\sigma_p - \sigma_f)\varphi}{(\sigma_p + 2\sigma_f) - (\sigma_p - \sigma_f)\varphi}\right)\sigma_f \tag{20}$$

The thermal conductivity of nanofluid is used according to the Maxwell model [49].

$$k_{nf} = k_f\left(\frac{k_p + 2k_f + 2\varphi(k_p - k_f)}{k_p + 2k_f - \varphi(k_p - k_f)}\right) \tag{21}$$

2.7. Physical and hydrodynamic properties

Average Nusselt numbers are calculated over the arc-shaped heater and defined as: [50].

$$Nu_{avg} = -\left(\frac{k_{nf}}{k_f} + \frac{4}{3}Rd\right)\int_S \frac{\partial\Theta}{\partial N}dS \tag{22}$$

The average velocity of the fluid is calculated as [51].

$$V_{avg} = \iint_A \frac{\sqrt{U^2 + V^2}}{A}dA \tag{23}$$

The average temperature of the domain is calculated as [51].

$$\Theta_{avg} = \iint_A \frac{\Theta}{A}dA \tag{24}$$

To construct the graphs of streamlines, the value of the stream function $\Psi(X, Y)$ has been used which is defined as, in non-dimensional form $U = \frac{\partial\Psi}{\partial Y}, V = -\frac{\partial\Psi}{\partial X}$ [48].

The positive value $\Psi(X, Y)$ indicates counterclockwise rotation of the flow and the negative value $\Psi(X, Y)$ indicates clockwise rotation of the flow of nanofluid.

3. Numerical methodology

3.1. Finite element algorithm

In this study, the algorithm utilized the Newton-Raphson method. To derive the discrete forms of the continuity, momentum, and energy equations, both a method and an algorithm were applied. The procedure was then employed to ascertain the values of velocity and temperature based on these equations. Predicting the initial values of the variables was crucial for determining potential outcomes. Following the calculations, numerical results were obtained, meeting the convergence criteria. The flowchart presented in Fig. 2 depicts the straightforward algorithm employed to solve this method.

3.2. Grid test

To decrease computing expense, non-uniform triangular elements were used to discretize the domain. Initially, a set of 882 triangular elements was taken into consideration, and thereafter, the number of elements was gradually augmented. The Nusselt number and temperature of the domain were computed for the augmented number of elements. The outcome is shown in Fig. 3. Based on the aforementioned study, it was determined that a total of 21,116 elements is the optimal amount for minimizing computing costs while still resulting in insignificant changes to the outcome. Fig. 4 depicts the process of generating a mesh for the physical model.

3.3. Code validation

To assess the precision, the existing numerical code is compared with the previously published research conducted by Khanafer and

Aithal [28]. This study aims to compare the characteristics of streamlines and isotherms, and the local *Nu* number along the bottom surface, in a cavity with a rotating cylinder under mixed convection conditions. Re is set to 100, Ri is set to 1, and the Prandtl number is set to 0.7. The findings are shown in Fig. 5. The comparison of the findings demonstrates a level of accuracy that is deemed adequate. The *Nu* number comparison, is carried out for several Ri = 0.1, 1, 5, 10, and two rotational speeds (ω = 10 and −10), and other parameters were kept fixed. This is illustrated by a line graph in Fig. 6, which shows the fine accuracy of the result.

4. Results and discussions

This portion discusses the impact of *Ha* on thermal performance and fluid flow in the square cavity with varying dimensionless time considering the constant Prandtl number (6.82), Reynolds number (100), Richardson number (1), solid volume fraction (4%), rotational speed of the cylinder (−5), and Radiation number (1). Different graphs, contours, and visualizations have been plotted such as streamlines, isotherms, average fluid velocity, average fluid temperature, and average Nusselt number.

4.1. Effect on streamlines

Fig. 7 depicts the velocity streamlines with magnitudes for four different Hartmann numbers (*Ha* = 0, 15, 30, 45) and various dimensionless times (0.1, 1, 2). When *Ha* = 0, no magnetohydrodynamics were considered, resulting in scattered velocity streamlines across the three dimensionless times. At dimensionless time = 0.1, the velocity profile created a cylindrical adjacent region, and a wake region appeared at the cavity's top side. However, with an increase in dimensionless time, the wake region was eliminated due to cylindrical rotations, and the velocity profiles were also scattered. A similar phenomenon was observed for *Ha* = 15 and 30, but the

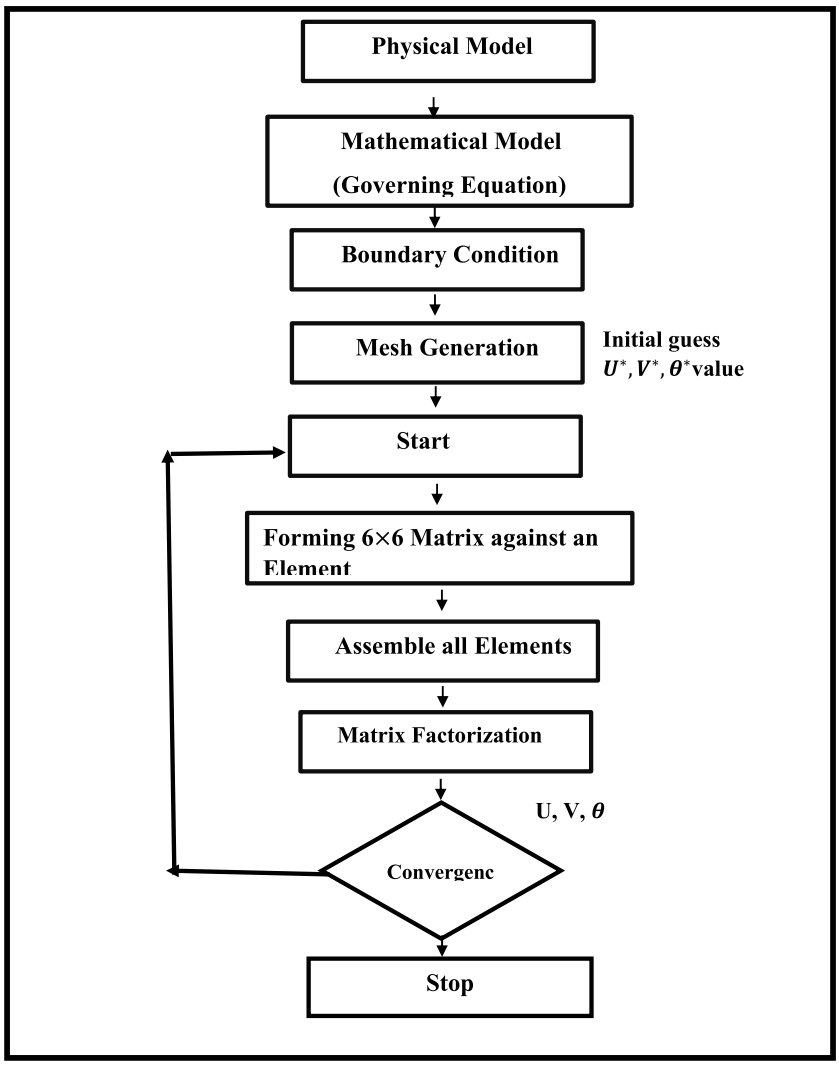

Fig. 2. Flowchart of the computational procedure.

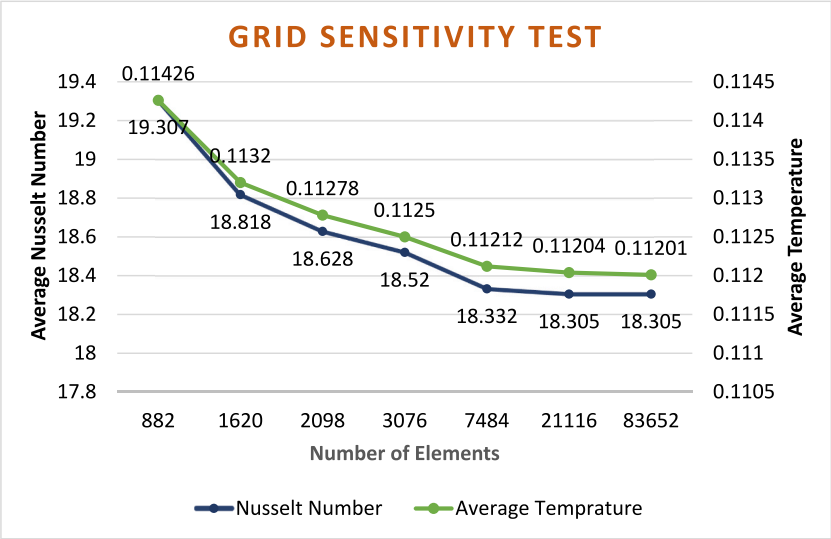

Fig. 3. Grid Sensitivity test.

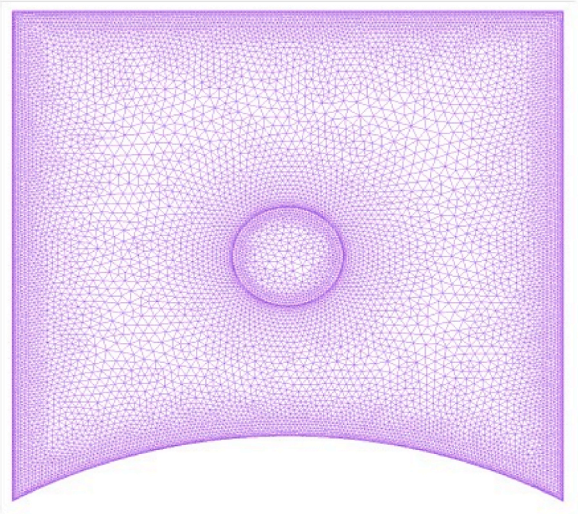

Fig. 4. Mesh generation of the physical model.

wake region remained for all dimensionless times in both cases due to the hindrance of fluid velocity flow by magnetohydrodynamics. The higher the presence of magnetohydrodynamics, the lower the velocity profile strength, resulting in the wake region staying in these cases. For $Ha = 45$, where the highest magnetohydrodynamics were present, the velocity profile effect was fragile. The wake region was present for all dimensionless times, and two wake regions with different magnitudes were formed at dimensionless times 1 and 2, situated one inside another. The presence of a magnetic field disrupts the fluid flow and has a significant impact on heat transfer, too.

4.2. *Effect on isotherm*

Heat is transmitted from the bottom curved wall to the fluid inside the cavity as a result of the existence of heat flux. The temperature distribution is shown by isotherm plots for different scenarios, as seen in Fig. 8. At a dimensionless time of 0.1, the temperature distribution is seen in the vicinity of the neighboring section of the bottom curved wall for all Hartmann number scenarios. However, the differentiation is not readily discernible in this particular dimensionless instance. However, the growth in dimensionless time reveals considerable effects in other circumstances without dimensions. As the spinning cylinder undergoes counterclockwise motion, the temperature distribution becomes more pronounced on the right side of the chamber. At a dimensionless time of 1, a little shoot emerges from the right corner of the hollow and thereafter ascends along the neighboring wall of the revolving cylinder located

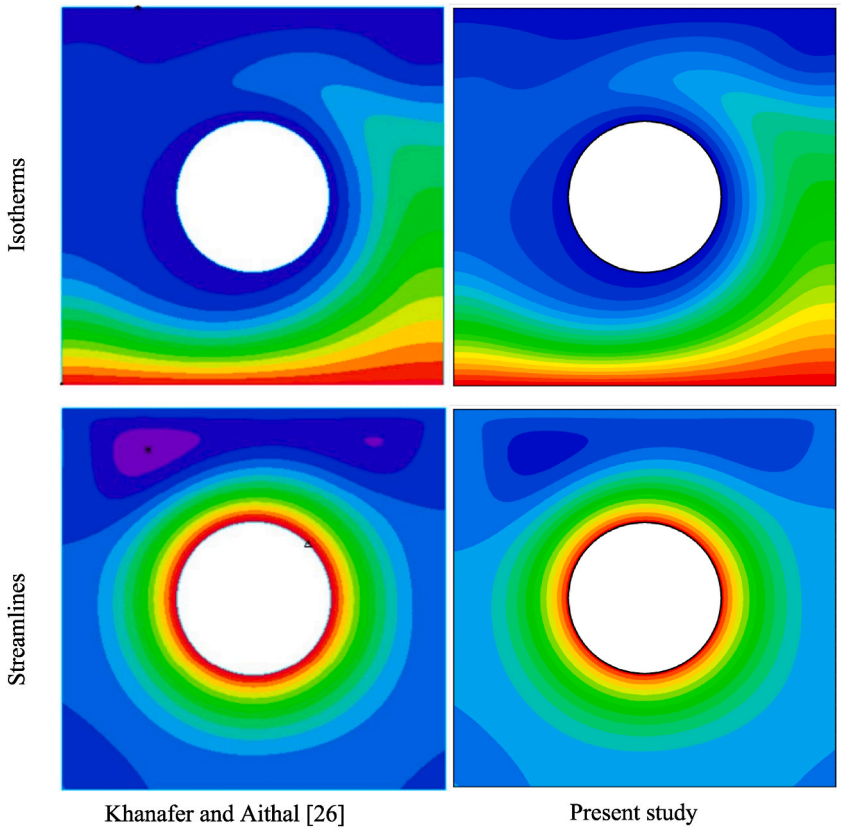

Fig. 5. Comparison of isotherms and streamlines with the previous study done by Khanafer and Aithal [26].

at the center of the cavity. These effects were seen in all examples of Hartmann numbers examined in this investigation. At a dimensionless time of 2, the temperature distribution attains its maximum value and propagates along the direction of fluid flow. The presence of magnetohydrodynamics is also apparent in the observed temperature differential. The relationship between the magnitude of the Hartmann number and the temperature distribution is such that a greater magnitude of the Hartmann number corresponds to lower temperature distributions. Consequently, the temperature distribution with the greatest magnitude is seen when magnetohydrodynamics is absent ($Ha = 0$) at a certain dimensionless time, and the lowest temperature distribution is observed when $Ha = 45$. The hindrance of fluid flow caused by magnetohydrodynamics leads to a decrease in heat dissipation inside the cavity.

4.3. Effect on average velocity of fluid for different Hartmann Number

The present investigation involves the use of a rotating cylinder positioned at the central region of the hollow, which undergoes continuous rotation at a constant velocity. Additionally, a moving lid is positioned at the upper wall. Therefore, the motion of the fluid may be characterized by its velocity. Fig. 9 illustrates the average velocity of the fluid inside the cavity is notably influenced by magnetohydrodynamics. Fig. 9 (a) presents a graphical representation showcasing the influence of Ha on the velocity at various dimensionless time intervals ranging from 0 to 2. A notable observation is that there is a substantial drop in the average fluid velocity as Ha rises. The adverse effects on the fluid dynamics inside the cavity may be attributed to the influence of magnetohydrodynamics. The scenario in which there is no magnetic influence ($Ha = 0$) has the greatest mean fluid velocity, measuring 0.82 in magnitude at a dimensionless time of 2. The scenario using $Ha = 45$ exhibits the minimum average velocity, measuring 0.28 in magnitude at a dimensionless duration of 2. The magnitudes corresponding to Hartmann numbers of 30 and 15 are 0.32 and 0.55, respectively. In addition, the mean fluid velocity experiences an upward trend as the dimensionless time grows over all Hartmann number scenarios. The differentiation of the average magnitude of fluid velocity for the four examples is not possible until dimensionless time 0.1. Nevertheless, the size exhibits a positive correlation with the augmentation of dimensionless time. For the scenarios where $Ha = 45$ and $Ha = 30$, the mean fluid velocity stays consistent beyond a certain dimensionless period. Nevertheless, when considering $Ha = 15$ and $Ha = 0$, it is shown that the average velocity exhibits a continuous rise as dimensionless time progresses. This phenomenon may be attributed to the inverse relationship between the Hartmann number and the level of impediment experienced by the fluid flow. Therefore, it may be concluded that the scenario where $Ha = 0$ exhibits the greatest mean fluid velocity. Fig. 9 (b) illustrates the same occurrence using an alternative visualization approach using a three-dimensional plot. Additionally, the average velocity of the fluid falls as the Hartmann number increases, whereas it increases significantly when the dimensionless time increases.

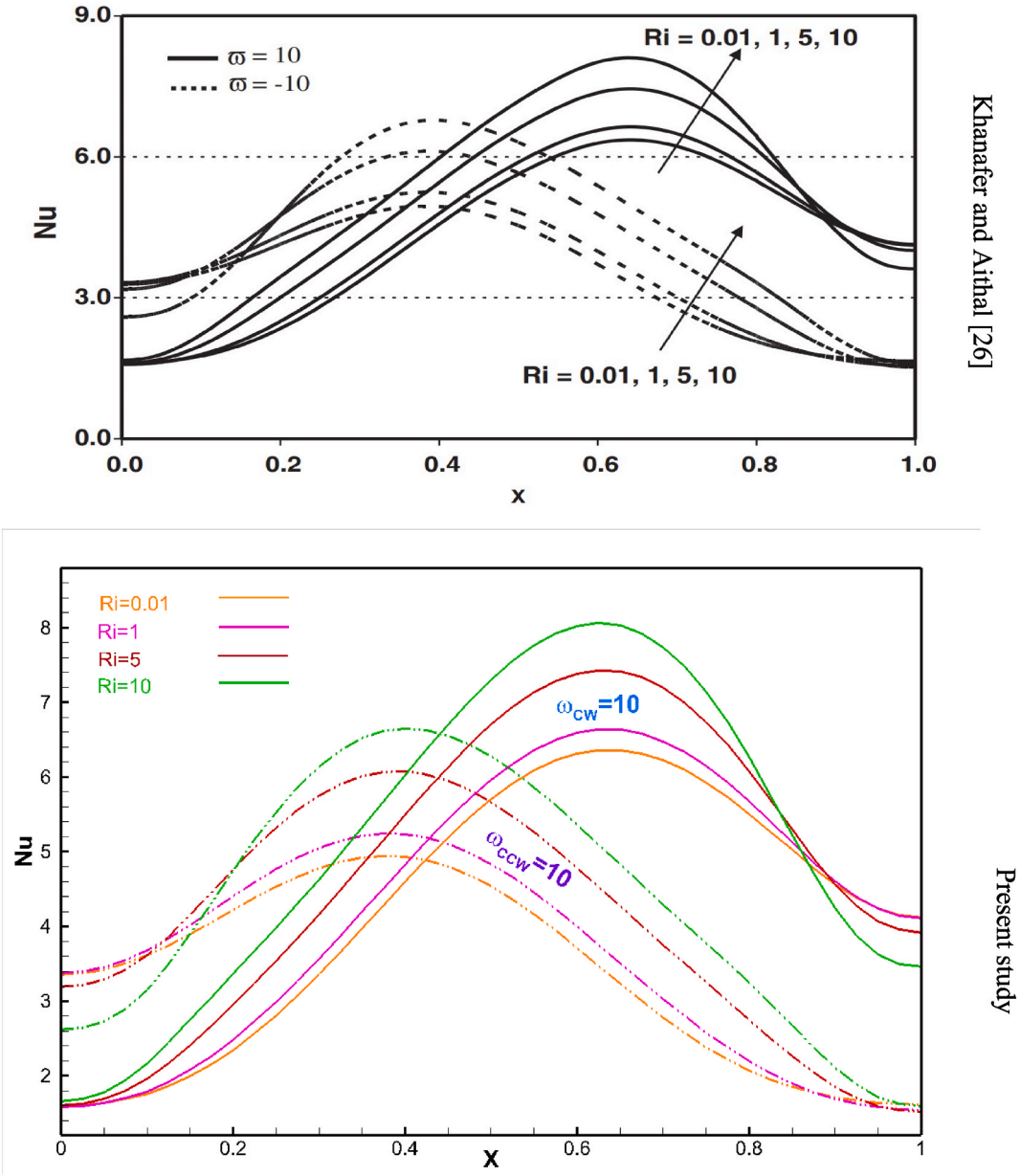

Fig. 6. Comparison of Local Nusselt number with the study of Khanafer and Aithal [26] and present study.

4.4. Average temperature of the fluid for different hartmann number

The non-uniform temperature distribution inside the cavity is attributed to the existence of a heat source, which is further affected by the presence of a centrally positioned revolving cylinder. Fig. 10 illustrates the influence of magnetohydrodynamics on the mean fluid temperature inside the cavity, as a function of dimensionless time, across various Hartmann number scenarios. Fig. 10 (a) illustrates the graphical representation of the average fluid temperature plotted against dimensionless time for four distinct situations of Hartmann number. The data reveals that there is a positive correlation between the fluid temperature and the dimensionless time. This correlation becomes more pronounced with larger dimensionless numbers for all the instances of Hartmann number. Hence, Fig. 10 (b) provides a magnified depiction of the graph, specifically emphasizing the situations with greater dimensionless numbers. The picture demonstrates a clear inverse relationship between the average fluid temperature and *Ha*. Specifically, as *Ha* lessens, the average fluid temperature increases. Because when there is lesser impact of magnetic field the fluid tends to flow freely inside the cavity and therefore the heat can dissipate easily. Notably, the example with $Ha = 0$ exhibits the highest average fluid temperature, measuring 0.114 in magnitude. The instance with a $Ha = 15$ exhibits the second-highest average fluid temperature, while the case with a $Ha = 45$ demonstrates the lowest average fluid temperature. The decrease in fluid temperature seen at higher Hartmann numbers may be

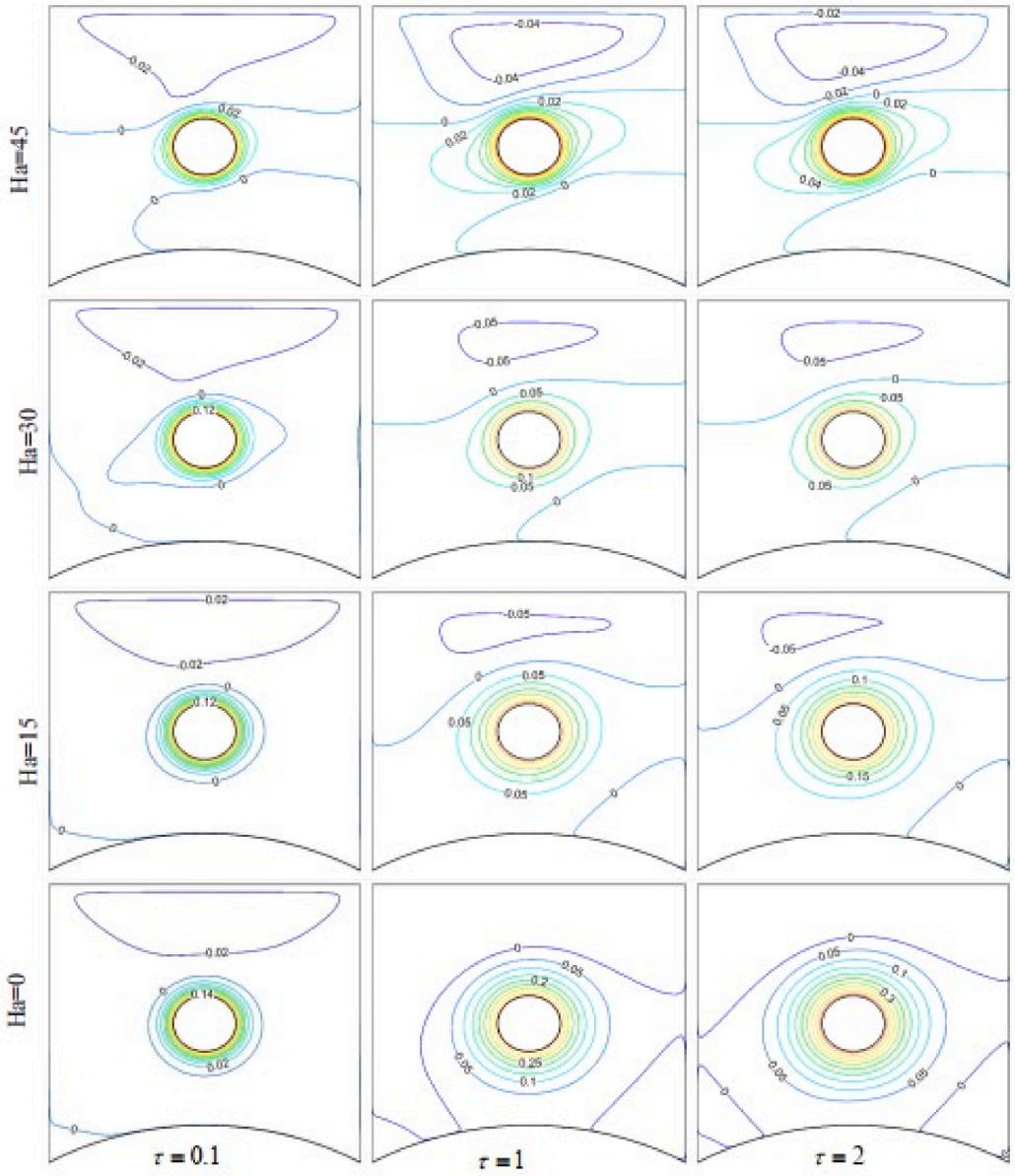

Fig. 7. Effect of Hartmann Number on Streamlines at different dimensionless times.

ascribed to the impediment imposed by magnetohydrodynamics, leading to a reduction in fluid velocity and influencing the dissipation of heat inside the cavity. Furthermore, Fig. 10 (c) illustrates a three-dimensional plot that depicts the same pattern, whereby the average fluid temperature augments as the dimensionless time increases and the Hartmann number decreases.

4.5. Effect on Average Nusselt number for different Hartmann Number

The Nusselt number is a non-dimensional heat transfer metric that establishes a relationship between the convective and the conductive heat transfer rate over a boundary layer. It refers to the convective-to-conductive heat transfer ratio. Fig. 11 depicts the impact of magnetohydrodynamics on the mean *Nu* inside the cavity across various Hartmann number scenarios, with dimensionless time serving as the independent variable. Fig. 11 (a) displays a graph depicting the average *Nu* as a function of dimensionless time for four distinct Hartmann number scenarios. *Nu* exhibits a decreasing trend as the dimensionless time increases across all the Hartmann number scenarios. This is because the magnetic field hinders the fluid flow and heat dissipation. Furthermore, when the Hartmann number increases, there is a corresponding drop in *Nu*. Therefore, the situation with $Ha = 0$, where magnetohydrodynamics is absent, exhibits the greatest average Nusselt number, while the case with $Ha = 45$ demonstrates the lowest Nusselt number. Distinguishing the

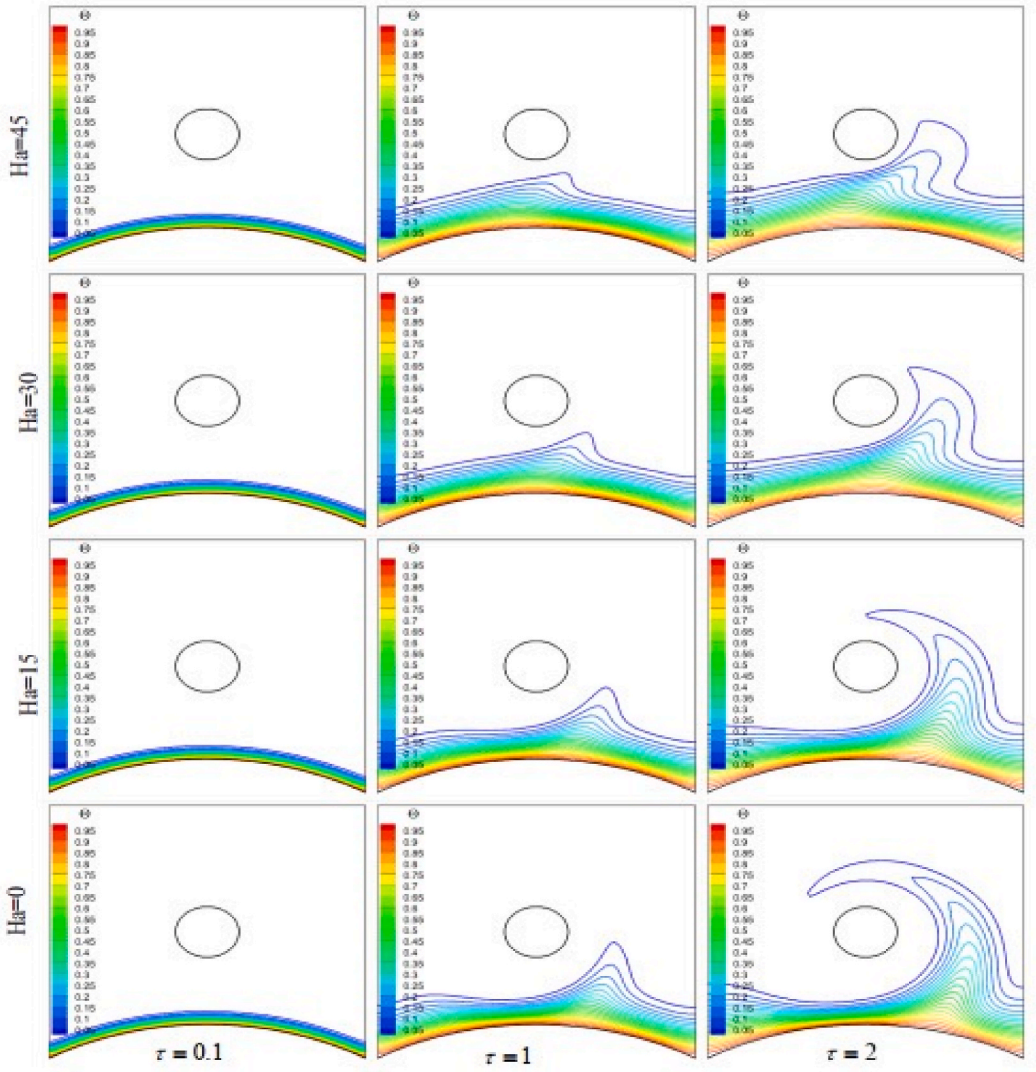

Fig. 8. Effect of Hartmann number on isotherms at different dimensionless time.

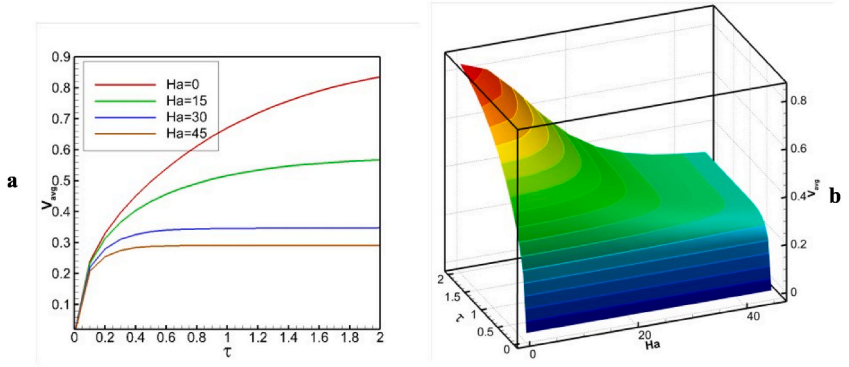

Fig. 9. Average velocity of fluid for different Hartmann number over dimensionless time.

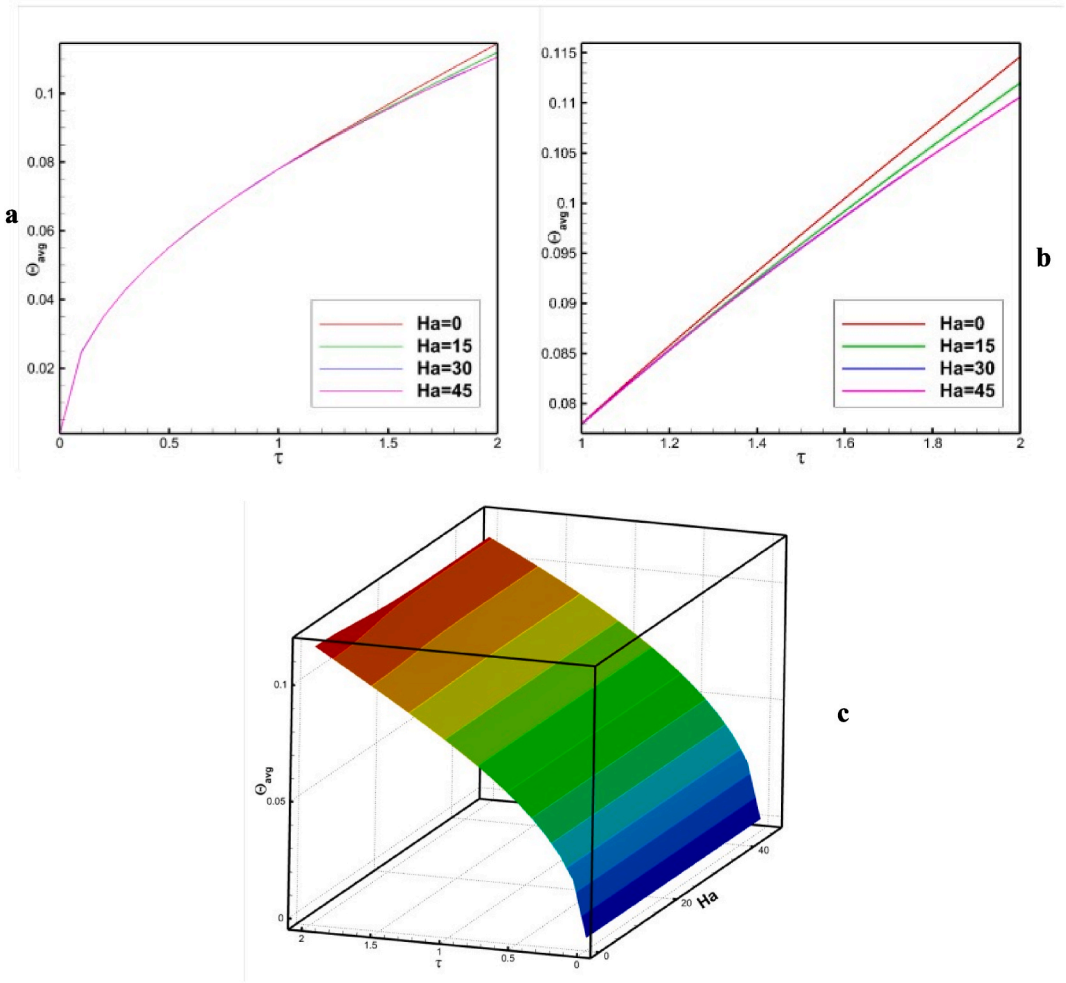

Fig. 10. Average temperature of the fluid for different Hartman number over the dimensionless time τ

variations among the Hartmann number situations becomes challenging during lower dimensionless timeframes. Nevertheless, beyond a dimensionless duration of 0.75, the disparities become more apparent. For every 0.1 s increase in time, heat transfer rate decreases exponentially. The amount of Nu_{av} can be modeled by the at $Ha = 0$, $Nu = 47.674e^{-0.252\tau}$, at $Ha = 15$, $Nu = 35.528e^{-0.187\tau}$, at $Ha = 30$, $Nu = 30.201e^{-0.154\tau}$, and at $Ha = 45$, $Nu = 29.681e^{-0.151\tau}$. On the other hand, as Ha increases from 0 to 15, Nu_{av} decreases by approximately 3.82%. From 15 to 30, it decreases by about 2.23%, and from 30 to 45, it decreases by about 0.05%. The 3D figure

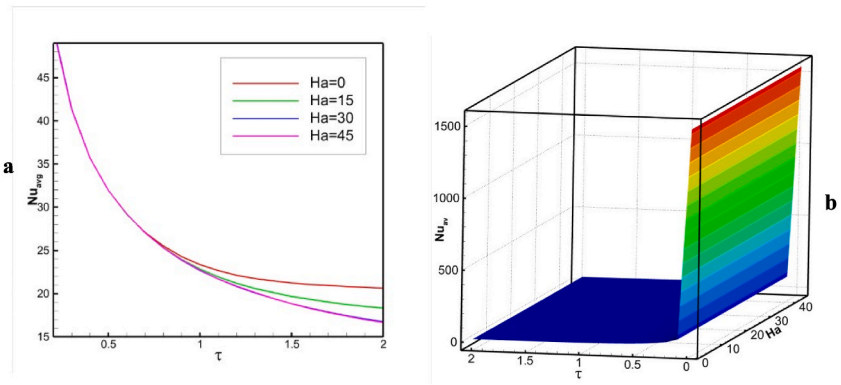

Fig. 11. Average Nusselt number for different Hartmann number over dimensionless time.

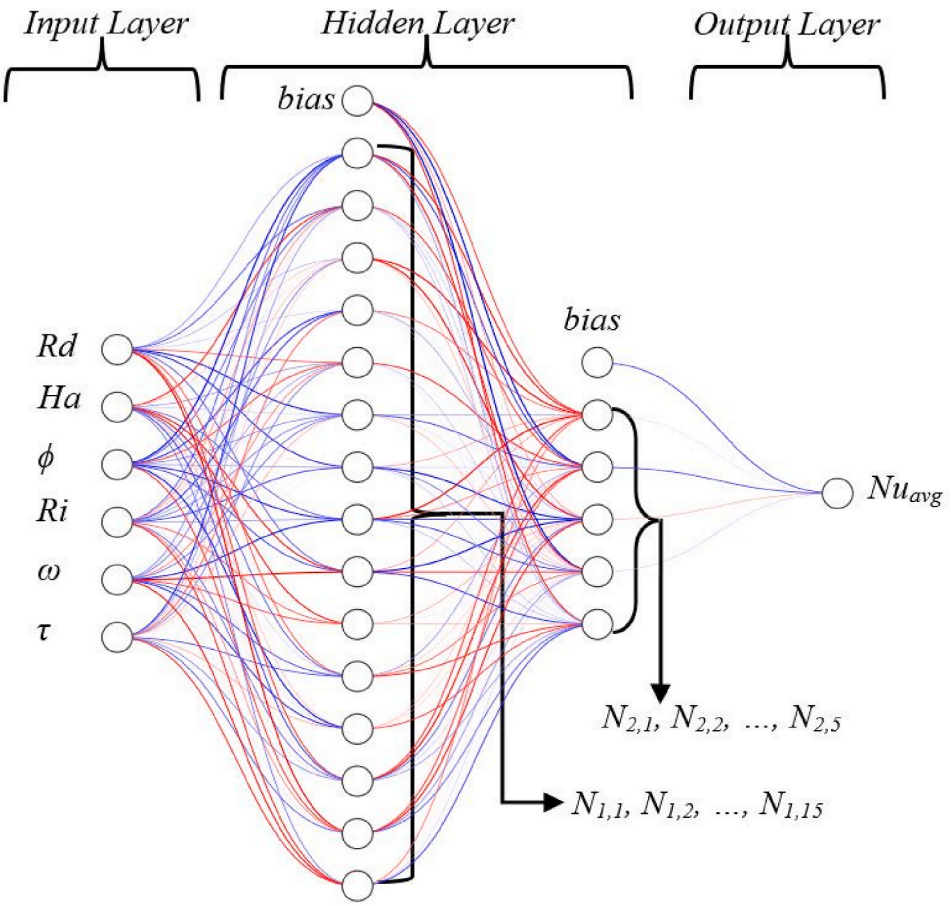

Model: "sequential"

Layer (type)	Output Shape	Param #
dense (Dense)	(None, 15)	105
dense_1 (Dense)	(None, 5)	80
dense_2 (Dense)	(None, 1)	6

Total params: 191 (764.00 Byte)
Trainable params: 191 (764.00 Byte)
Non-trainable params: 0 (0.00 Byte)

Fig. 12. ANN diagram (top) and number of parameters solved in ANN model (bottom).

shown in Fig. 11 (b) exhibits similar patterns, indicating that *Nu* declines as the dimensionless number rises and *Ha* increases.

5. Artificial neural network analysis

An artificial neural network (ANN) is a computer framework that emulates the functioning of the human brain, enabling the modeling of complex patterns and the resolution of prediction problems. The process of establishing a relationship between a set of numerical inputs and a corresponding set of numerical objectives is accomplished via the use of a neural network. An ANN may possess a range of architectural configurations, including feed-forward, recurrent, multi-layer, or single-layer designs. The ANN structure shown in Fig. 12 has three layers: the input layer, the hidden layer, and the output layer. The used model was a feed-forward back-propagation neural network, since feed-forward networks are well-suited for solving finite input-output mapping problems. To forecast the output variable (Nu_s), a dataset consisting of 6144 entries for the six input variables (Ra, *Ha*, φ, Ri, τ, ω) is used.

The figure presented depicts the schematic graph of the Artificial Neural Network (ANN) model, located at the top, and the number of parameters that have been resolved inside each layer of the ANN model is illustrated in the bottom graph. This investigation involved the use of two hidden layers with the objective of enhancing the functionality of the hidden layer. The second concealed layer comprises five neurons, whereas the first concealed layer comprises fifteen neurons. In light of the lack of a predetermined approach to determining the ideal number of hidden layers. Two hidden layers are used inside this particular framework to enhance operational effectiveness and address the complexity of the model.

5.1. Training, testing, and finding of the model

In this study, we used the total number of observations (6144), 4300 observations, or 70% of the total data, are used as train data, while 1844 observations, or 30% of the data, are used as test data. For this study, a wide range of parameters were taken into consideration to analyze of the behavior of the Nusselt number. Here, the values of the variables were considered as *Ha* (10, 20, 30, 40), Rd (1, 2, 3.5, 5), φ (0.01, 0.05, 0.1, 0.15), ω (1, 2, 5, 10), Ri (0.01, 1, 5, 10), τ (0, 0.4, 0.8, 1.2, 1.6, 2), and others parameters were kept fixed. The network is employed to predict Nu_{avg} and evaluate model accuracy using the mean square error (MSE), mean absolute error (MAE), and mean absolute percentage error (MAPE). The network under consideration is trained using the Levenberg-Marquardt backpropagation technique, as described in Ref. [52]. This research examines the use of the Rectified Linear Unit (ReLU) as the transfer function for the first hidden layers, the Tangent Hyperbolic function as the transfer function for the second hidden levels, and a linear transfer function for the output layer.

$$MSE = \frac{1}{n}\sum_{i=1}^{n}(Nu_s - Nu_A)^2 \tag{25}$$

$$MAE = \frac{\sum_{i=1}^{n}|Nu_s - Nu_A|}{n} \tag{26}$$

$$MAPE = \frac{1}{n}\sum_{i=1}^{n}\left|\frac{Nu_s - Nu_A}{Nu_s}\right| \tag{27}$$

$$ReLU : f(x) = \max(0, x) \tag{28}$$

$$Tanh : \tanh(x) = \frac{2}{1 + e^{-2x}} - 1 \tag{29}$$

Here, Nu_A stands for ANN Nusselt (predicted output data), Nu_S for simulated Nusselt (input data), and n for data size or number of observations.

The activation functions that were employed in the hidden layers are found in equations (28) and (29) according to Sharma et al. [53], while the MSE, MAE, and MAPE are found in equations (25)–(27) based on Rana et al. [54].

Fig. 13 illustrates the relationship between the loss function, specifically the mean absolute error (MAE), and the number of epochs. In this instance, the model underwent initial training with a batch size of 20 and a total of 100 epochs. However, according to the preceding image, it is evident that a mere 15–20 epochs of data would suffice. Finally, a total of 20 epochs were used to predict the data. The Mean Squared Error (MSE) value is calculated to be 0.00069, while the Mean Absolute Error (MAE) value is determined to be 0.0175. Furthermore, the accuracy of the model, as measured by the Mean Absolute Percentage Error (MAPE), is 99.0225, equivalent to 99.02%. The following data is a random selection of predicted test results. Table 2 presents the projected data and the Absolute Percentage Error (APE) associated with the forecasted data. Furthermore, the data supplied is presented randomly and is considered to be test data.

6. Conclusions

The primary objective of this computational study was to analyze the heat transfer mechanisms and fluid dynamics occurring in an

arc-shaped cavity with a lid-driven motion, where the cavity was filled with a nanofluid consisting of water and Al_2O_3 nanoparticles. The research investigated the effect of manipulating the Hartmann number while keeping the Richardson number, Radiation parameter, solid volume percentage, and Reynolds number constant. Furthermore, a cylindrical object was positioned in the central region of the hollow. The Levenberg-Marquardt backpropagation method is used to train artificial neural networks (ANNs) utilizing sparse simulated data. The findings of the research are shown via the use of streamlines, isotherms, mean fluid velocity, mean fluid temperature, and mean Nusselt number. The Hartmann number was changed over four distinct values ($Ha = 0, 15, 30, 45$), whereas the dimensionless time was varied across three distinct values ($\tau = 0.1, 1, 2$). The primary outcomes of this investigation are succinctly outlined as follows.

- The velocity profile exhibits a positive correlation with the augmentation of dimensionless time. Moreover, an upper cavity zone experiences the formation of a wake region of greater magnitude as the *Ha* augments. The strength of the velocity profile diminishes as the intensity of magnetohydrodynamics rises.
- The temperature distribution lessens as the size of the Hartmann number augments as a result of the impediment to fluid motion. The temperature distribution exhibits its maximum value when the magnetohydrodynamics parameter (*Ha*) is set to zero, at a certain dimensionless time. Conversely, the minimum temperature distribution is seen when *Ha* is equal to 45.
- When the Hartmann number is increased, there is a corresponding drop in the average fluid velocity at a certain dimensionless time. The scenario in which there is no magnetic influence ($Ha = 0$) has the greatest average fluid velocity, measuring 0.82 in magnitude at a dimensionless time of 2. The scenario in which $Ha = 45$ exhibits the lowest average velocity, measuring 0.28 in magnitude at a dimensionless time of 2.
- The scenario in which there is no magnetic influence ($Ha = 0$) has the greatest average fluid velocity, measuring 0.82 in magnitude at a dimensionless time of 2. The scenario in which $Ha = 45$ has the smallest mean velocity, measuring 0.28 in magnitude at a dimensionless period of 2. The fluid temperature increases as the Hartmann number decreases, reaching its maximum value for the $Ha = 0$ condition, with a magnitude of 0.114.
- The average fluid temperature increases as the Hartmann number decreases, reaching its maximum value of 0.114 for the situation of $Ha = 0$. The situation with $Ha = 0$, indicating the absence of magnetohydrodynamics, exhibits the greatest average Nusselt number, whilst the case with $Ha = 45$ demonstrates the lowest Nusselt number.
- Among the total of 6144 data, a subset of 4300 observations was used to train a two-layer feed-forward back propagation sequential model, while the remaining 1844 observations were reserved for assessing the performance of the model. The model has a level of accuracy of 99.02%. In this research, a neural network model was used to predict the average Nusselt number using six input factors and one output variable. The results indicate that the artificial neural network achieved a prediction accuracy of 99%.

The major limitation of the study lies in having convergence issues while considering higher Hartmann numbers. Future research can be focused on introducing more inlets and in the cavity, changing the shape of the lower wall, such as the wavy-shaped wall, and incorporating various hybrid nanofluids, etc.

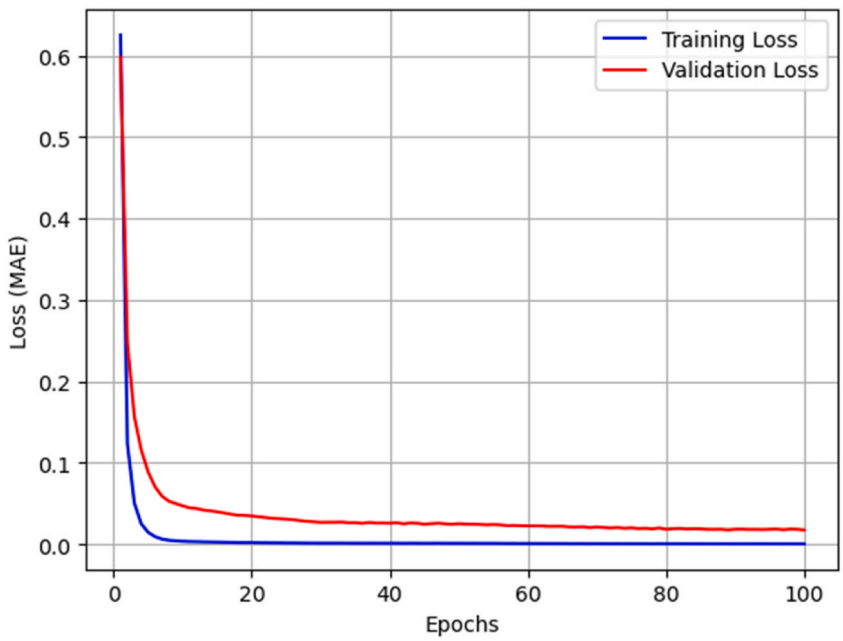

Fig. 13. MAE vs Epochs graph.

Table 2
Predicted data using test data

Rd	*Ha*	φ	ω	Ri	τ	Nu_S	Nu_A	APE
1	20	0.05	5	1	0.4	37.64669	37.5351	0.296414
1	20	0.05	5	5	1.6	20.5724	20.582333	0.048273
1	40	0.1	1	5	0.4	38.58906	38.861073	0.7049
1	20	0.1	2	0.01	1.6	19.47232	19.86337	2.008244
1	30	0.15	10	5	1.6	25.45538	25.23289	0.874049
1	20	0.01	5	0.01	0	61.95251	61.428986	0.845044
1	40	0.01	2	1	1.6	18.52084	18.65151	0.705555
1	30	0.01	2	10	0.4	36.97659	37.17709	0.542242
2	40	0.01	10	10	0.8	33.09696	32.709034	1.172097
2	40	0.1	2	10	2	22.03396	22.495035	2.092561
2	40	0.05	5	0.01	1.6	23.85363	24.132832	1.170479
2	40	0.1	1	10	1.6	23.89318	23.866884	0.110072
2	20	0.1	10	5	0.4	47.43996	46.998962	0.929589
2	40	0.05	10	0.01	1.6	24.48259	24.577114	0.386072
2	20	0.1	10	1	2	29.98087	29.915127	0.219298
2	40	0.15	5	5	1.2	28.70792	29.007221	1.042561
2	30	0.15	10	0.01	0.8	36.96582	36.419353	1.478301
2	30	0.05	1	1	0	71.55415	71.20994	0.481051
2	30	0.1	10	0.01	0.8	34.63347	34.2111	1.219537
2	40	0.1	10	0.01	0	72.38014	71.88551	0.683367
2	30	0.1	5	1	0.8	33.64714	33.716934	0.20744
2	30	0.1	2	5	1.2	27.29603	27.45605	0.586256
3.5	40	0.1	10	0.01	0.4	57.96407	57.400803	0.971746
3.5	30	0.15	2	1	0.4	58.32126	58.31947	0.003073
3.5	10	0.01	5	10	1.6	37.88677	38.01296	0.333075
3.5	20	0.01	2	1	2	25.98848	26.297539	1.189212
3.5	30	0.05	2	10	0.4	57.4103	57.475986	0.114419
3.5	30	0.05	2	0.01	0	82.37191	82.00699	0.44302
3.5	40	0.01	2	0.01	1.6	28.49308	28.480665	0.04356
5	10	0.05	5	10	0.8	49.14191	49.33013	0.383023

CRediT authorship contribution statement

T. Bairagi: Formal analysis. **Md Jahid Hasan:** Writing – original draft. **M.N. Hudha:** Formal analysis. **A.K. Azad:** Writing – review & editing, Validation. **M.M. Rahman:** Supervision.

Declaration of competing interest

The authors declare that they have no known competing financial interests or personal relationships that could have appeared to influence the work reported in this paper.

References

[1] S. Yeasmin, Z. Islam, A.K. Azad, E.M.M. Alam, M.M. Rahman, M.F. Karim, Thermal performance of a hollow cylinder with low conductive materials in a lid-driven square cavity with partially cooled vertical wall, Therm. Sci. Eng. Prog. 35 (2022) 101454, https://doi.org/10.1016/J.TSEP.2022.101454.
[2] M. Azeez, K. Al-farhany, N. Mahjoub, M.A. Flayyih, Numerical investigation of double-diffusive mixed convection in a split lid-driven curvilinear cavity, Int. Commun. Heat Mass Tran. 138 (2022) 106322, https://doi.org/10.1016/j.icheatmasstransfer.2022.106322.
[3] A.I. Alsabery, M.H. Yazdi, A.S. Abosinnee, I. Hashim, E. Solomin, Impact of partial slip condition on mixed convection of nano fl uid within lid-driven wavy cavity and solid inner body, Propuls. Power Res. 11 (4) (2022) 544–564, https://doi.org/10.1016/j.jppr.2022.09.001.
[4] D. Kashyap, A.K. Dass, Influence of cavity inclination on mixed convection in a double-sided lid-driven cavity with a centrally inserted hot porous block Lattice Boltzmann method, Int. J. Therm. Sci. 181 (April) (2022) 107732, https://doi.org/10.1016/j.ijthermalsci.2022.107732.
[5] D.T. Yaseen, S.M. Salih, M.A. Ismael, Effect of the lid-driven on mixed convection in an open flexible wall cavity with a partially heated bottom wall, Int. J. Therm. Sci. 188 (February) (2023) 108213, https://doi.org/10.1016/j.ijthermalsci.2023.108213.
[6] S. Yeasmin, M.M. Billah, Z. Molla, K.E. Hoque, Numerical analysis of unsteady mixed convection heat transfer characteristics of nanofluids confined within a porous lid-driven L-shaped cavity, Int. J. Thermofluids 16 (September) (2022) 100218, https://doi.org/10.1016/j.ijft.2022.100218.
[7] H. Zhang, et al., Numerical study of mixed convection and entropy generation of Water-Ag nanofluid filled semi- elliptic lid-driven cavity, Alex. Eng. J. 61 (11) (2022) 8875–8896, https://doi.org/10.1016/j.aej.2022.02.028.
[8] A. Wang, H. Xu, Highly accurate wavelet-homotopy solutions for mixed convection hybrid nanofluid flow in an inclined square lid-driven cavity, Comput. Math. Appl. 108 (September 2021) (2022) 88–108, https://doi.org/10.1016/j.camwa.2022.01.004.
[9] S. Hussain, A.M. Aly, H.F. Oztop, Magneto-bioconvection flow of hybrid nanofluid in the presence of oxytactic bacteria in a lid-driven cavity with a streamlined obstacle 134 (April) (2022), https://doi.org/10.1016/j.icheatmasstransfer.2022.106029.
[10] S. Batool, G. Rasool, N. Alshammari, I. Khan, H. Kaneez, Numerical analysis of heat and mass transfer in micropolar nanofluids flow through lid driven cavity : finite volume approach Nomenclature, Case Stud. Therm. Eng. 37 (June) (2022) 102233, https://doi.org/10.1016/j.csite.2022.102233.
[11] S. Ahmed, H. Xu, Y. Zhou, Q. Yu, Modelling convective transport of hybrid nanofluid in a lid driven square cavity with consideration of Brownian diffusion and thermophoresis, Int. Commun. Heat Mass Tran. 137 (2022) 106226, https://doi.org/10.1016/j.icheatmasstransfer.2022.106226.
[12] S. Das, B. Tarafdar, R.N. Jana, O.D. Makinde, Influence of wall CONDUCTIVITES on a fully developed mixed-convection magnetohydrodynamic nanofluid 91 (3) (2018) 784–796, https://doi.org/10.1007/s10891-018-1801-4.

[13] M. Farooq, M.I. Khan, M. Waqas, T. Hayat, A. Alsaedi, M.I. Khan, MHD Stagnation Point Fl Ow of Viscoelastic Nano Fl Uid with Non-linear Radiation Effects, vol. 221, 2016, pp. 1097–1103, https://doi.org/10.1016/j.molliq.2016.06.077.

[14] A. Mostafazadeh, D. Toghraie, Effect of radiation on laminar natural convection of nanofluid in a vertical channel with single- and two-phase approaches, J. Therm. Anal. Calorim. 2 (2019), https://doi.org/10.1007/s10973-019-08236-2.

[15] M. Sheikholeslami, T. Hayat, A. Alsaedi, On simulation of nanofluid radiation and natural convection in an enclosure with elliptical cylinders, Int. J. Heat Mass Transf. 115 (2017) 981–991, https://doi.org/10.1016/j.ijheatmasstransfer.2017.07.119.

[16] M. Sheikholeslami, Magnetic field influence on nanofluid thermal radiation in a cavity with tilted elliptic inner cylinder, J. Mol. Liq. (2016), https://doi.org/10.1016/j.molliq.2016.12.024.

[17] F.A. Soomro, R.U. Haq, Q.M. Al-mdallal, Q. Zhang, Heat generation/absorption and nonlinear radiation effects on stagnation point flow of nanofluid along a moving surface, Results Phys. (2017), https://doi.org/10.1016/j.rinp.2017.12.037.

[18] P. Barnoon, D. Toghraie, R. Balali, H. Abed, MHD mixed convection and entropy generation in a lid-driven cavity with rotating cylinders fi lled by a nano fl uid using two phase mixture model, J. Magn. Magn Mater. 483 (March) (2019) 224–248, https://doi.org/10.1016/j.jmmm.2019.03.108.

[19] E. Çolak, H.F. Öztop, Ö. Ekici, MHD Mixed Convection in a Chamfered Lid-Driven Cavity with Partial Heating, vol. 156, 2020, https://doi.org/10.1016/j.ijheatmasstransfer.2020.119901.

[20] Z. Korei, S. Benissaad, F. Berrahil, A. Filali, MHD mixed convection and irreversibility analysis of hybrid nanofluids in a partially heated lid-driven cavity chamfered from the bottom side, Int. Commun. Heat Mass Tran. 132 (2022) 105895, https://doi.org/10.1016/j.icheatmasstransfer.2022.105895.

[21] R. Nasrin, S. Parvin, Hydromagnetic effect on mixed convection in a lid-driven cavity with sinusoidal corrugated bottom surface, Int. Commun. Heat Mass Tran. 38 (6) (2011) 781–789, https://doi.org/10.1016/j.icheatmasstransfer.2011.03.002.

[22] F. Selimefendigil, H.F. Öztop, MHD mixed convection of nanofluid in a flexible walled inclined lid-driven L-shaped cavity under the effect of internal heat generation, Physica A 534 (2019) 122144, https://doi.org/10.1016/j.physa.2019.122144.

[23] S. Das, N. Mahato, A. Ali, R.N. Jana, Dynamical behaviour of magneto-copper-titania/water-ethylene glycol stream inside a gyrating channel, Chem. Phys. Lett. 793 (February) (2022) 139476, https://doi.org/10.1016/j.cplett.2022.139476.

[24] S. Das, N. Mahato, A. Ali, R.N. Jana, Aspects of Arrhenius kinetics and Hall currents on gyratory Couette flow of magnetized ethylene glycol containing bi-hybridized nanomaterials, Heat Transf. 52 (4) (2023) 2995–3026, https://doi.org/10.1002/htj.22814.

[25] A. Shafiq, A.B. Çolak, T.N. Sindhu, Development of an intelligent computing system using neural networks for modeling bioconvection flow of second-grade nanofluid with gyrotactic microorganisms, Numer. Heat Transf. Part B Fundam. 0 (0) (2023) 1–18, https://doi.org/10.1080/10407790.2023.2273512.

[26] D. Chatterjee, S. Kumar, B. Mondal, Mixed convective transport in a lid-driven cavity containing a nano fl uid and a rotating circular cylinder at the center, Int. Commun. Heat Mass Tran. 56 (2014) 71–78, https://doi.org/10.1016/j.icheatmasstransfer.2014.06.002.

[27] A. Khaleel, S. Gao, Mixed convection heat transfer of turbulent flow in a three-dimensional lid-driven cavity with a rotating cylinder, Int. J. Heat Mass Transf. 112 (2017) 185–200, https://doi.org/10.1016/j.ijheatmasstransfer.2017.04.118.

[28] K. Khanafer, S.M. Aithal, Mixed convection heat transfer in a lid-driven cavity with a rotating circular cylinder, Int. Commun. Heat Mass Tran. 86 (2017) 131–142, https://doi.org/10.1016/j.icheatmasstransfer.2017.05.025.

[29] A. Imtiaz, J. Mahmud, R. Hossain, S. Saha, Annals of Nuclear Energy Influence of heat generation/absorption on mixed convective flow in a lid-driven chamber with isothermal rotating cylinder, Ann. Nucl. Energy 182 (November 2022) (2023) 109596, https://doi.org/10.1016/j.anucene.2022.109596.

[30] F. Selimefendigil, H.F. Oztop, Mixed convection of ferro fl uids in a lid driven cavity with two rotating cylinders m (2015) 439–451, https://doi.org/10.1016/j.jestch.2015.03.003.

[31] A. Shafiq, A. Batur Çolak, T. Naz Sindhu, S. Ahmad Lone, A. Alsubie, F. Jarad, Comparative study of artificial neural network versus parametric method in COVID-19 data analysis, Results Phys. 38 (May) (2022) 105613, https://doi.org/10.1016/j.rinp.2022.105613.

[32] A. Shafiq, A.B. Çolak, T.N. Sindhu, Analyzing activation energy and binary chemical reaction effects with artificial intelligence approach in axisymmetric flow of third grade nanofluid subject to soret and dufour effects, Heat Transf. Res. 54 (3) (2023) 75–94, https://doi.org/10.1615/HeatTransRes.2022045008.

[33] A. Shafiq, A.B. Çolak, T.N. Sindhu, Significance of EMHD graphene oxide (GO) water ethylene glycol nanofluid flow in a Darcy–Forchheimer medium by machine learning algorithm, Eur. Phys. J. Plus 138 (3) (2023), https://doi.org/10.1140/epjp/s13360-023-03798-5.

[34] A. Shafiq, A.B. Çolak, T.N. Sindhu, Modeling of soret and dufour's convective heat transfer in nanofluid flow through a moving needle with artificial neural network, Arab. J. Sci. Eng. 48 (3) (2023) 2807–2820, https://doi.org/10.1007/s13369-022-06945-9.

[35] A. Shafiq, A.B. Çolak, T.N. Sindhu, Q.M. Al-Mdallal, T. Abdeljawad, Estimation of unsteady hydromagnetic Williamson fluid flow in a radiative surface through numerical and artificial neural network modeling, Sci. Rep. 11 (1) (2021) 1–21, https://doi.org/10.1038/s41598-021-93790-9.

[36] A.B. Çolak, T.N. Sindhu, S.A. Lone, A. Shafiq, T.A. Abushal, Reliability study of generalized Rayleigh distribution based on inverse power law using artificial neural network with Bayesian regularization, Tribol. Int. 185 (December 2022) (2023) 108544, https://doi.org/10.1016/j.triboint.2023.108544.

[37] A. Shafiq, A.B. Çolak, T.N. Sindhu, Comparative analysis to study the Darcy–Forchheimer Tangent hyperbolic flow towards cylindrical surface using artificial neural network: an application to Parabolic Trough Solar Collector, Math. Comput. Simul. 216 (2024) 213–230, https://doi.org/10.1016/j.matcom.2023.09.014.

[38] A. Shafiq, A.B. Çolak, T.N. Sindhu, S.A. Lone, T.A. Abushal, Modeling and survival exploration of breast carcinoma: a statistical, maximum likelihood estimation, and artificial neural network perspective, Artif. Intell. Life Sci. 4 (April) (2023) 100082, https://doi.org/10.1016/j.ailsci.2023.100082.

[39] T.N. Sindhu, A.B. Çolak, S.A. Lone, A. Shafiq, Reliability study of generalized exponential distribution based on inverse power law using artificial neural network with Bayesian regularization, Qual. Reliab. Eng. Int. 39 (6) (2023) 2398–2421, https://doi.org/10.1002/qre.3352.

[40] A. Shafiq, A.B. Çolak, T.N. Sindhu, Reliability investigation of exponentiated Weibull distribution using IPL through numerical and artificial neural network modeling, Qual. Reliab. Eng. Int. 38 (7) (2022) 3616–3631, https://doi.org/10.1002/qre.3155.

[41] A. Shafiq, A.B. Çolak, T.N. Sindhu, Modeling of Darcy-Forchheimer magnetohydrodynamic Williamson nanofluid flow towards nonlinear radiative stretching surface using artificial neural network, Int. J. Numer. Methods Fluids 95 (9) (2023) 1502–1520, https://doi.org/10.1002/fld.5216.

[42] A. Shafiq, A.B. Çolak, T.N. Sindhu, Optimization of the numerical treatment of the Darcy–Forchheimer flow of Ree–Eyring fluid with chemical reaction by using artificial neural networks, Int. J. Numer. Methods Fluids 95 (1) (2023) 176–192, https://doi.org/10.1002/fld.5147.

[43] A. Shafiq, A.B. Çolak, T. Naz Sindhu, Designing artificial neural network of nanoparticle diameter and solid–fluid interfacial layer on single-walled carbon nanotubes/ethylene glycol nanofluid flow on thin slendering needles, Int. J. Numer. Methods Fluids 93 (12) (2021) 3384–3404, https://doi.org/10.1002/fld.5038.

[44] M.J. Hasan, A.K. Azad, R. Hossain, M.M. Rahman, M.F. Karim, Analysis of mixed convection under radiation and magnetohydrodynamics utilizing Kerosene-CNT nanofluid in a lid-driven cavity, Int. J. Thermofluids 21 (2024) 100528, https://doi.org/10.1016/j.ijft.2023.100528.

[45] R. Hossain, A.K. Azad, M. Jahid Hasan, M.M. Rahman, Thermophysical properties of Kerosene oil-based CNT nanofluid on unsteady mixed convection with MHD and radiative heat flux, Eng. Sci. Technol. an Int. J. 35 (2022) 101095, https://doi.org/10.1016/j.jestch.2022.101095.

[46] M.H. Hasib, M.S. Hossen, S. Saha, Effect of tilt angle on pure mixed convection flow in trapezoidal cavities filled with water-Al2O3 nanofluid, Procedia Eng. 105 (2015) 388–397, https://doi.org/10.1016/j.proeng.2015.05.024.

[47] M.J.H. Sagor, A.B.M.R. Hasan, S. Saha, Entropy analysis due to conjugate natural convection in water-Al2O3 nanofluid filled prismatic cavity, AIP Conf. Proc. 2324 (1) (2021) 50022, https://doi.org/10.1063/5.0037522.

[48] M.A. Taghikhani, Cu–Water nanofluid MHD mixed convection in a lid-driven cavity with two sinusoidal heat sources considering joule heating effect, Int. J. Thermophys. 40 (4) (2019) 44, https://doi.org/10.1007/s10765-019-2507-3.

[49] A.K. Azad, M.M. Shuvo, R.H. Kabir, K.M. Rabbi, M.F. Karim, M.M. Rahman, Heat transfer augmentation in a diamond shaped enclosure utilizing CNT-water Nanofluid, Int. Commun. Heat Mass Tran. 116 (2020) 104647, https://doi.org/10.1016/j.icheatmasstransfer.2020.104647.

[50] K. Khanafer, K. Vafai, A critical synthesis of thermophysical characteristics of nanofluids, Int. J. Heat Mass Transf. 54 (19–20) (2011) 4410–4428, https://doi.org/10.1016/J.IJHEATMASSTRANSFER.2011.04.048.

[51] M. Abul, K. Azad, MHD Combined Convection in a Channel with Cavity Using Nanofluids, 2016.

[52] H. Yu, B.M.W.S.E. L. Training, Levenberg—marquardt training, in: The Industrial Electronics Handbook, CRC Press, 2011, https://doi.org/10.1201/b10604-15.
[53] S. Sharma, S. Sharma, A. Athaiya, Activation functions in neural networks, Towar. Data Sci 6 (12) (2017) 310–316.
[54] P. Rana, A. Kumar, G. Gupta, Impact of different arrangements of heated elliptical body, fins and differential heater in MHD convective transport phenomena of inclined cavity utilizing hybrid nanoliquid: artificial neutral network prediction, Int. Commun. Heat Mass Tran. 132 (2022) 105900.